

Abundances of sulphur molecules in the Horsehead nebula

First NS⁺ detection in a photodissociation region

P. Rivière-Marichalar^{1,2}, A. Fuente², J. R. Goicoechea¹, J. Pety^{3,4}, R. Le Gal⁵, P. Gratier⁶, V. Guzmán⁷, E. Roueff⁸, J. C. Loison⁹, V. Wakelam⁶, M. Gerin⁴

¹ Instituto de Física Fundamental (CSIC), Calle Serrano 121, 28006 Madrid, Spain e-mail: p.riviere@oan.es

² Observatorio Astronómico Nacional (OAN,IGN), Apdo 112, E-28803 Alcalá de Henares, Spain

³ Institut de Radioastronomie Millimétrique (IRAM), 300 rue de la Piscine, 38406 Saint Martin d'Hères, France

⁴ LERMA, Observatoire de Paris, PSL Research University, CNRS, Sorbonne Universités, UPMC Univ. Paris 06, Ecole Normale Supérieure, F-75005 Paris, France

⁵ Harvard-Smithsonian Center for Astrophysics, 60 Garden St., Cambridge, MA 02138, USA

⁶ Laboratoire d'Astrophysique de Bordeaux, Univ. Bordeaux, CNRS, B18N, allée Geoffroy Saint-Hilaire, 33615 Pessac, France

⁷ Instituto de Astrofísica, Pontificia Universidad Católica de Chile, Av. Vicuña Mackenna, 4860, 7820436, Macul, Santiago, Chile

⁸ LERMA, Observatoire de Paris, PSL Research University, CNRS, Sorbonne Universités, UPMC Univ. Paris 06, F-92190 Meudon, France

⁹ Institut des Sciences Moléculaires de Bordeaux (ISM), CNRS, Univ. Bordeaux, 351 cours de la Libération, 33400, Talence, France

ABSTRACT

Context. Sulphur is one of the most abundant elements in the Universe ($S/H \sim 1.3 \times 10^{-5}$) and plays a crucial role in biological systems on Earth. The understanding of its chemistry is therefore of major importance.

Aims. Our goal is to complete the inventory of S-bearing molecules and their abundances in the prototypical photodissociation region (PDR) the Horsehead nebula to gain insight into sulphur chemistry in UV irradiated regions. Based on the WHISPER (Wide-band High-resolution Iram-30m Surveys at two positions with Emir Receivers) millimeter (mm) line survey, our goal is to provide an improved and more accurate description of sulphur species and their abundances towards the core and PDR positions in the Horsehead

Methods. The Monte Carlo Markov Chain (MCMC) methodology and the molecular excitation and radiative transfer code RADEX were used to explore the parameter space and determine physical conditions and beam-averaged molecular abundances.

Results. A total of 13 S-bearing species (CS, SO, SO₂, OCS, H₂CS – both ortho and para – HDCS, C₂S, HCS⁺, SO⁺, H₂S, S₂H, NS and NS⁺) have been detected in the two targeted positions. This is the first detection of SO⁺ in the Horsehead and the first detection of NS⁺ in any PDR. We find a differentiated chemical behaviour between C-S and O-S bearing species within the nebula. The C-S bearing species C₂S and o-H₂CS present fractional abundances a factor of > two higher in the core than in the PDR. In contrast, the O-S bearing molecules SO, SO₂, and OCS present similar abundances towards both positions. A few molecules, SO⁺, NS, and NS⁺, are more abundant towards the PDR than towards the core, and could be considered as PDR tracers.

Conclusions. This is the first complete study of S-bearing species towards a PDR. Our study shows that CS, SO, and H₂S are the most abundant S-bearing molecules in the PDR with abundances of \sim a few 10^{-9} . We recall that SH, SH⁺, S, and S⁺ are not observable at the wavelengths covered by the WHISPER survey. At the spatial scale of our observations, the total abundance of S atoms locked in the detected species is $< 10^{-8}$, only $\sim 0.1\%$ of the cosmic sulphur abundance.

Key words. Astrochemistry – ISM: abundances – ISM: kinematics and dynamics – ISM: molecules – stars: formation – stars: low-mass

1. Introduction

Sulphur is one of the most abundant elements in the Universe ($S/H \sim 1.3 \times 10^{-5}$ in the solar photosphere, Asplund et al. 2005) and plays a crucial role in biological systems on Earth. Surprisingly, sulphuretted molecules are not as abundant as expected in the interstellar medium. A few sulphur compounds have been detected in diffuse clouds demonstrating that the sulphur abundance in these low density regions is close to the cosmic value (Neufeld

et al. 2015). A moderate sulphur depletion (a factor of four) is estimated in the external layers of the photodissociation region (PDR) in the Horsehead nebula (Goicoechea et al. 2006). In cold molecular clouds, a large depletion of sulphur is usually considered to reproduce the observations (see for instance Tieftrunk et al. 1994; Vastel et al. 2018). The depletion of sulphur is observed not only in cold pre-stellar cores, but also in hot cores/corinos (Wakelam et al. 2004). One would expect that most of the sulphur is locked in the icy grain mantles in dense cores but we should see almost

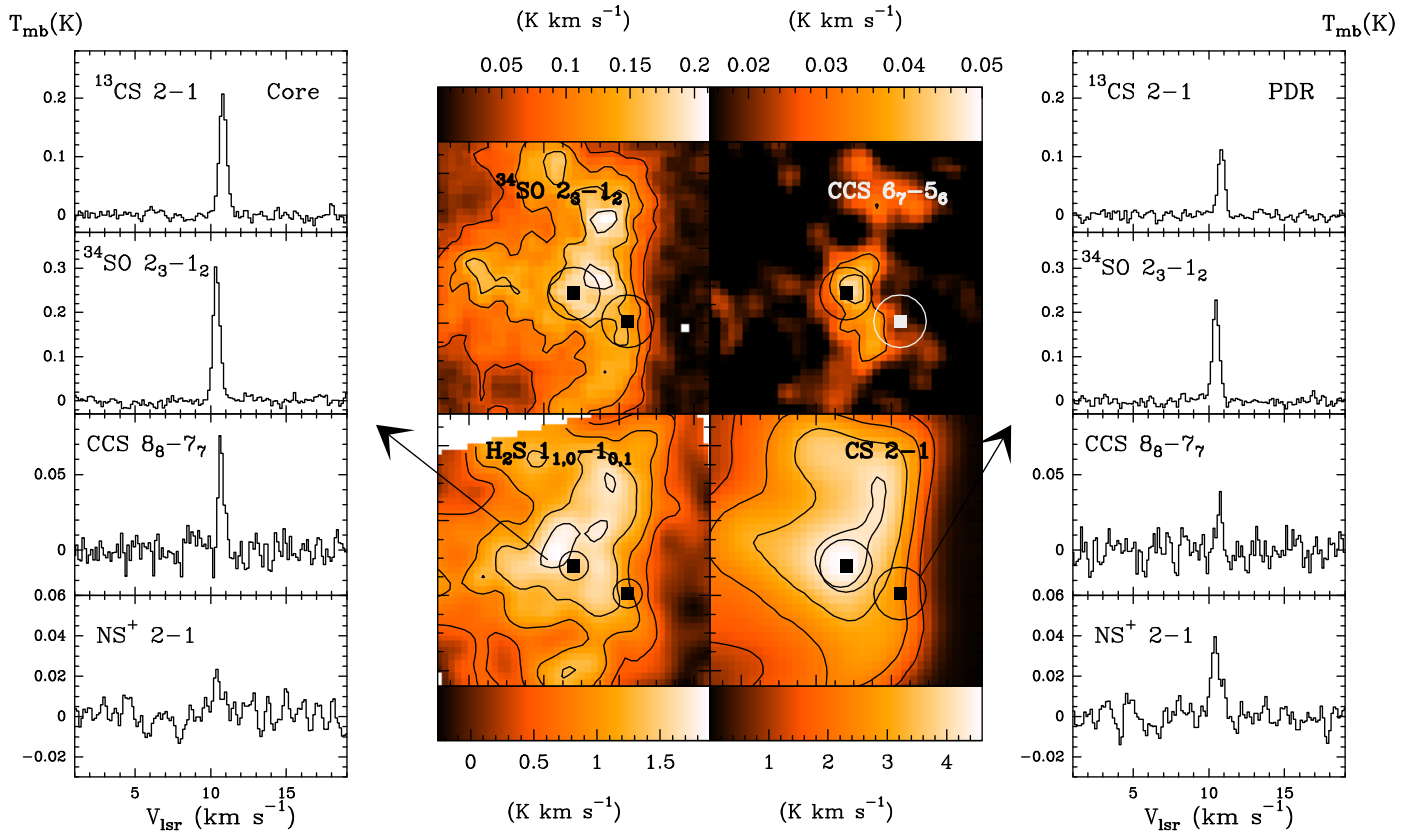


Fig. 1. Integrated intensity maps of the $^{13}\text{CS } 2\rightarrow 1$, $^{34}\text{SO } 2_3\rightarrow 1_2$, $\text{CCS } 8_7\rightarrow 7_6$, and $\text{H}_2\text{S } 1_{1,0}\rightarrow 1_{0,1}$ maps as observed with the 30m IRAM telescope. The beam of the 30m telescope at 3mm (HPBW $\sim 29''$) is indicated by two circles centred on the positions targeted within the Whisper spectral survey. Line contours depict 30 to 90 by 15% levels with respect to the emission peak.

all sulphur return to the gas phase in hot cores and strong shocks. However, even in the well-known Orion–KL hot core where the icy grain mantles are expected to evaporate releasing the molecules to the gas phase, one needs to assume a sulphur depletion of a factor of approximately ten to reproduce the observations (Esplugues et al. 2014; Crockett et al. 2014). Because of the high hydrogen abundances and the mobility of hydrogen in the ice matrix, sulphur atoms impinging on interstellar ice mantles are expected to form H_2S preferentially. However, there are only upper limits of the solid H_2S abundance (e.g. Jiménez-Escobar & Muñoz Caro 2011). Oba et al. (2018) show that, at high densities, chemical desorption is likely to exceed photodesorption, thus becoming an efficient way of removing H_2S from the surface of grains.

Thus far, OCS is the only S-bearing molecule unambiguously detected in interstellar ice because of its large band strength in the infrared (Geballe et al. 1985; Palumbo et al. 1995); tentatively, SO_2 has also been detected (Boogert et al. 1997). The bulk of the S-budget might be locked in atomic sulphur in the gas phase and/or in S-polymers in the solid phase, which are not easily observable (Jiménez-Escobar et al. 2014; Wakelam et al. 2004). The recent detection of the doubly-sulphuretted species S_2H in the Horsehead nebula adds important information as well as new questions to the overall complex sulphur chemistry problem, possibly supporting the scenario of an important role of surface chemistry in the formation of the gaseous sul-

phuretted compounds (Fuente et al. 2017). Observations of the comet 67P with Rosetta showed that H_2S and atomic S are the most important S-bearing species in cometary ices, with an abundance of 0.015 % relative to water (Calmonte et al. 2016; Bockelée-Morvan & Biver 2017).

Only a few PDRs have been investigated in detail taking advantage of their proximity and favourable edge-on geometry: NGC 7023 (Fuente et al. 1993, 1996, 2000), the Orion Bar (Cuadrado et al. 2015, 2017; Goicoechea et al. 2016, 2017), Mon R2 (Ginard et al. 2012; Treviño-Morales et al. 2014, 2016; Pilleri et al. 2012, 2013, 2014), and the Horsehead nebula. Here we investigate the sulphur chemistry in the Horsehead nebula. At a distance of 400 pc, the Horsehead is a PDR viewed nearly edge-on and illuminated by the O9.5V star σOri at a projected distance of ~ 3.5 pc. The intensity of the incident far ultra-violet (FUV) radiation field is $\chi=60$ (Pety et al. 2005) relative to the interstellar radiation field in Draine units (Draine 1978). This PDR presents a differentiated chemistry from others associated with warmer regions such as the Orion Bar, NGC 7023, and Mon R2. One main difference is that the dust temperature is around $\sim 20\text{--}30$ K in the PDR (Goicoechea et al. 2009), meaning it is below or close to the sublimation temperature of many species, allowing a rich surface chemistry on the irradiated surfaces as has been demonstrated by recent observational and theoretical studies (Guzmán et al. 2011, 2013). A first analysis of the sulphur chemistry was carried out by Goicoechea et al. (2006) who derived a gas-phase

sulphur abundance of $S/H=(3.5\pm 1.5)\times 10^{-6}$ in the low extinction PDR on the basis of single-dish and interferometric observations of the CS and HCS⁺ millimeter lines.

The Horsehead Wide-band High-resolution Iram-30m Surveys at two positions with Emir Receivers (WHISPER) project is a complete unbiased line survey of the 3, 2, and 1 mm bands using the Institut de Radioastronomie Millimétrique (IRAM) 30m telescope. WHISPER has provided valuable hints regarding the chemistry of this region. The detection of the molecular ion CF⁺ towards the HCO peak is well understood in terms of gas-phase photochemistry (Guzmán et al. 2012). Photo-destruction of large polyatomic molecules or small grains into smaller hydrocarbon precursors is invoked to explain the extraordinarily high abundance of small hydrocarbons, such as C₂H, C₃H₂, C₃H, and C₃H⁺ (Pety et al. 2012; Guzmán et al. 2015). The detection of several complex organic molecules (COMs) towards the warm ($T_{\text{kin}} \sim 60$ K) PDR was unexpected. In fact, the chemical complexity reached in the Horsehead is surprisingly high, with COMs of up to seven atoms: HCOOH, H₂CCO, CH₃CHO, and CH₃CCH (Guzmán et al. 2014). Current pure gas-phase models cannot reproduce the inferred H₂CO, CH₃OH, and COMs abundances in the Horsehead PDR (Guzmán et al. 2011, 2013), which supports the theory of a grain surface origin for these molecules. Le Gal et al. (2017) were able to reproduce the observed COMs abundances using a chemical model with grain surface chemistry and proposed that chemical desorption, instead of photodesorption, was most likely the dominant process to release COMs to the gas phase. However, the efficiency of chemical desorption seems to be extremely dependent on the species involved and the chemical composition of the icy mantle (Minissale et al. 2016; Oba et al. 2018). CH₃CN and CH₃NC, key species for the formation of prebiotic molecules, seem to have a very specific formation pathway in this PDR (Gratier et al. 2013). In this paper we use the data of the Horsehead WHISPER project to investigate the chemistry of S-bearing species in this prototypical nebula.

2. Observations and data reduction

The data used in this work are taken from the Horsehead WHISPER (Wide-band High-resolution Iram-30m Surveys at two positions with Emir Receivers, PI: J. Pety) project. The Horsehead WHISPER project is a complete unbiased line survey of the 3, 2, and 1 mm bands using the IRAM 30m telescope. Two positions were observed within this survey: i) the PDR position, where HCO emission peaks (RA=5^h40^m53^s.936, Dec=02°28'00", J2000) at the UV-illuminated surface of the Horsehead nebula (Gerin et al. 2009a, hereafter, PDR), and ii) the core, where DCO⁺ peaks (RA=5^h40^m55^s.61, Dec=02°27'38", J2000), which corresponds to a cold ($T_k \sim 10-20$ K, Pety et al. 2007) and UV-shielded condensation located less than 40" away from the PDR edge (hereafter, core). During the observations we used the position-switching procedure with the reference position located at an offset (-100",0) relative to RA: 05^h40^m54^s.27 Dec: -02°28'00".0. In order to avoid relative calibration errors we integrated towards the HCO peak and the DCO⁺ peak alternatively, changing from one position to the other every 15 minutes. Line intensities are given in main brightness temperature (T_{MB}) and the frequency res-

olution in our survey is 49 kHz. The uncertainties in T_{MB} due to calibration errors are $\sim 10\%$.

In Fig. 1, we show the integrated intensity maps of the ³⁴SO 2₃→1₂, CCS 8₇→7₆, H₂S 1_{1,0}→1_{0,1}, and CS 2→1 lines as observed with the IRAM 30m telescope. These maps were observed in previous projects by our team. The two targeted positions within WHISPER, PDR and core, are marked with filled squares and the 3mm and 2mm beam of the 30m telescope are also shown. The H₂S 1_{1,0}→1_{0,1} line has been presented in Fuente et al. (2017). The other lines were observed in November and December 2017 under good winter weather conditions (2 mm of precipitable water vapour) using the Eight MIXer Receiver (EMIR) sideband-separation receivers. The position-switching, on-the-fly observing mode was used, with off-position offsets ($\delta\text{RA}, \delta\text{Dec} = (-100'', 0'')$), that is, into the HII region. We observed along and perpendicular to the direction of the exciting star in zigzags, covering an area of 200" × 200". The maps were processed with the Grenoble Image and Line Data Analysis System (GILDAS¹) software (Pety et al. 2005). The data were first calibrated to the T_{a}^* scale using the chopper-wheel method (Penzias & Burrus 1973), and then converted into main-beam temperatures (T_{mb}) using the forward and main-beam efficiencies of the telescope. The resulting spectra were then baseline-corrected and gridded through convolution with a Gaussian to obtain the maps. Beam sizes are roughly in the range 12" to 25", depending on the exact frequency of each transition, more precisely, $\text{HPBW}('') = 2460/\nu(\text{GHz})^2$.

3. Molecular inventory

Taking the high sensitivity WHISPER survey as the observational basis, we have systematically searched for all the S-bearing species included in the Cologne Database for Molecular Spectroscopy (CDMS) catalogue. A complete list of intensities for the detected lines is provided in Table A.1. Figure A.1 depicts the spectra of the detected transitions grouped by species. For the detected species, we have carried out a multi-transitional study that includes lines of different isotopologues, to determine accurate molecular abundances (Tables 1, and 4). In the case of non-detections, an upper limit to the fractional abundance is given. The list of non-detected species is shown in Table 3. A detailed description of the methods used to derive molecular abundances can be found in Sects. 4 and 5.

The list of S-bearing species detected in the Horsehead includes CS, SO, SO₂, OCS, H₂CS (both ortho- and para-), HDCS, C₂S, HCS⁺, SO⁺, H₂S, S₂H, NS, and NS⁺. The detections of H₂S and S₂H were previously reported by Fuente et al. (2017). It is important to note that this list constitutes the most complete inventory of S-bearing species in a PDR thus far. We have not detected DCS⁺ and CCCS towards any of the observed positions, and we provide upper limits for the fractional abundance of these molecules. The detection of NS⁺ reported here is worth noticing as the first detection of NS⁺ in a PDR. NS⁺ was recently identified by Cernicharo et al. (2018) in a variety of dark clouds, with a NS/NS⁺ $\sim 30-50$. However, a NS/NS⁺ > 3000 was mea-

¹ See <http://www.iram.fr/IRAMFR/GILDAS> for more information about the GILDAS softwares.

² See http://www.iram.es/IRAMES/telescope/telescope_Summary/telescope_summary.html.

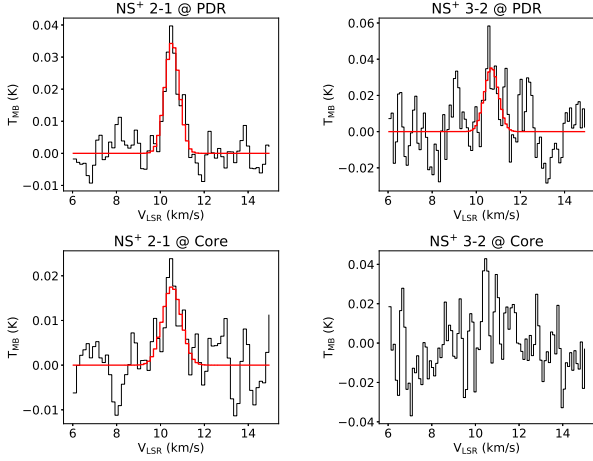


Fig. 2. Spectra of NS^+ in the PDR and the core. The red line shows the Gaussian fit to the observed line profile.

sured in the Orion KL hot core (Cernicharo et al. 2018). We have detected two NS^+ lines, $J=2\rightarrow 1$ at 110198.5 MHz and $J=3\rightarrow 2$ at 150295.6 MHz, with a signal-to-noise ratio (S/N) >4 towards the PDR position. Only the line at 110198.5 MHz has been detected towards the core (see Fig. 2).

We present also the first detection of SO^+ in a low-UV PDR ($\chi < 500$). Detected earlier by Turner (1992), SO^+ has been detected in variety of regions, which include massive star formation regions, shocked regions, and translucent clouds (Turner 1992, 1994, 1996). Although widely detected, a high abundance of SO^+ relative to SO , $X(\text{SO}^+)/X(\text{SO}) > 100$, seems to be related to photon-dominated chemistry and was proposed by Sternberg & Dalgarno (1995) as a tracer of UV illuminated regions. These high SO^+ abundances have been previously measured in the PDRs associated to NGC 7023 (Fuente et al. 2003), the Orion Bar (Fuente et al. 2003; Goicoechea et al. 2017), and Monoceros R 2 (Ginard et al. 2012), but this ion has not been detected in a low-UV PDR such as the Horsehead thus far.

4. Rotational diagrams

We have used the rotational diagram technique to derive rotational temperatures, T_{rot} , and beam-averaged column densities, $N(X)$. The results are summarized in Table 1. This method assumes that the population of the molecular energy levels can be characterized by a single temperature, T_{rot} , and that this temperature is uniform along the line of sight. Given the large beam sizes in our observations ($\sim 12''$ at 200 GHz to $\sim 25''$ at 100 GHz), the assumption of a single T_{rot} for each molecule and position is an oversimplification, yet a valid starting point for our analysis. We also assume that the emission from the different species is filling the beam. While this is most likely the case for many species (see Fig. 1), it might bias our results in some cases.

In its simplest formulation, assuming optically thin emission and the Rayleigh-Jeans limit, the rotation temperature and molecular column density can be derived from the equations

$$\ln\left(\frac{N_{up}}{g_{up}}\right) = \ln\left(\frac{N_{tot}}{Q_{rot}}\right) - \frac{E_{up}}{kT_{rot}} \quad (1)$$

$$N_{up}(\text{cm}^{-2}) = 1.94 \times 10^3 \nu^2 (\text{GHz}) W / A_{ul} (\text{s}^{-1}), \quad (2)$$

where W is the velocity-integrated line area in units of K km s^{-1} . We assume that the emission is extended compared with the beam size, that is, there is beam filling factor of 1, and consider only $\text{S/N}(\text{Area}) > 5$ detections to compute rotational diagrams.

The assumption of optically thin emission cannot be applied to the abundant species CS and SO . In these cases, we use the expression

$$\ln\left(\frac{N_{up}^{obs}}{g_{up}}\right) = \ln\left(\frac{N_{tot}^{obs}}{Q_{rot}}\right) - \frac{E_{up}}{kT_{rot}} - \ln(C_{\tau}), \quad (3)$$

with

$$C_{\tau} = \frac{\tau}{1 - e^{-\tau}} \quad (4)$$

being the optical depth correction factor (Goldsmith & Langer 1999). Line opacities, τ , are derived for each individual line assuming $^{12}\text{C}/^{13}\text{C} = 60$ and $^{32}\text{S}/^{34}\text{S} = 22.5$ (Wilson & Rood 1994). For a few species, we detected only one transition and we need to assume a certain T_{rot} to estimate column densities. Based on the results of the rotational diagrams of molecules with similar dipole moments (Table 1 and Fuente et al. 2017; Goicoechea et al. 2006), we assume $T_{\text{rot}} = 10$ K in these cases. The same rotational temperature is used to calculate the 3σ column density upper limits shown in Table 3.

5. RADEX models

We used the molecular excitation code RADEX (van der Tak et al. 2007) to get a more detailed description of the physical conditions and molecular abundances at the two positions observed. RADEX is a non-Local Thermodynamic Equilibrium (LTE) molecular excitation and local radiative transfer code that provides line intensities of molecular species for a given combination of T_k , n_{H_2} , and $N(X)$. We used a Monte Carlo Markov chain (MCMC) methodology to explore the parameter space using a Bayesian inference approach. Specifically, we used the *emcee* (Foreman-Mackey et al. 2012) implementation of the Affine Invariant MCMC Ensemble sampler methods by Goodman & Weare (2010).

When several isotopologues of the same species were detected, as is the case for CS and SO , all the isotopologues were modelled simultaneously assuming the isotopic ratios $^{13}\text{C}/^{12}\text{C} = 60$ and $^{34}\text{S}/^{32}\text{S} = 22.5$. Based on our previous knowledge of the region and previous studies by the WHISPER team (Gratier et al. 2013), we decided to assume a Gaussian prior for the kinetic temperature, with mean value and standard deviation $T_k = 60 \pm 10$ K in the PDR and $T_k = 25 \pm 10$ K in the core, and a log-normal prior for the gas density with mean value and standard deviation $\log_{10}(n_{\text{H}_2}[\text{cm}^{-3}]) = 4.8 \pm 0.2$ in the PDR and $\log_{10}(n_{\text{H}_2}[\text{cm}^{-3}]) = 5.0 \pm 0.2$ in the core. We assumed a flat prior for column densities between 10^9 cm^{-2} and 10^{15} cm^{-2} . An overview of the collisional partners and collisional excitation rates used for the different species modelled is shown in Table 2. For SO transitions, collisional

Table 1. Rotational temperatures, column densities, and abundances derived from rotational diagrams for S-bearing species in the Horsehead nebula.

Species	PDR			Core		
	T_{rot} (K)	$N(X)$ (cm^{-2})	Abundance $\frac{N(X)}{N(H)+2N(H_2)}$	T_{rot} (K)	$N(X)$ (cm^{-2})	Abundance $\frac{N(X)}{N(H)+2N(H_2)}$
CS*	6.3	$(3.0\pm 0.6)\times 10^{13}$	$(8.0\pm 2.0)\times 10^{-10}$	5.9	$(5.3\pm 1.0)\times 10^{13}$	$(9.0\pm 2.0)\times 10^{-10}$
SO*	11.6	$(3.2\pm 0.3)\times 10^{13}$	$(8.4\pm 0.8)\times 10^{-10}$	8.2	$(5.0\pm 0.5)\times 10^{13}$	$(8.6\pm 0.9)\times 10^{-10}$
p-H ₂ CS	4.2	$(5.0\pm 3.0)\times 10^{11}$	$(1.3\pm 0.8)\times 10^{-11}$	8.6	$(9.0\pm 1.0)\times 10^{11}$	$(1.6\pm 0.2)\times 10^{-11}$
o-H ₂ CS	8.8	$(9.0\pm 3.0)\times 10^{11}$	$(2.4\pm 0.8)\times 10^{-11}$	8.2	$(2.5\pm 0.8)\times 10^{12}$	$(4.3\pm 1.4)\times 10^{-11}$
SO ₂	6.5	$(3.0\pm 0.6)\times 10^{12}$	$(8.0\pm 1.6)\times 10^{-11}$	6.9	$(2.9\pm 0.6)\times 10^{12}$	$(5.0\pm 1.0)\times 10^{-11}$
CCS	10.3	$(3.0\pm 1.0)\times 10^{11}$	$(8.0\pm 2.6)\times 10^{-12}$	8.1	$(1.5\pm 0.7)\times 10^{12}$	$(2.6\pm 1.2)\times 10^{-11}$
HCS ⁺	11.6	$(5.0\pm 0.6)\times 10^{11}$	$(1.3\pm 0.2)\times 10^{-11}$	10**	6×10^{11}	1.0×10^{-11}
SO ⁺	11	$(6.3\pm 1.8)\times 10^{11}$	$(1.7\pm 0.5)\times 10^{-11}$	9	$(4.5\pm 0.5)\times 10^{11}$	$(7.8\pm 0.9)\times 10^{-12}$
HDCS	10**	$(6\pm 1)\times 10^{11}$	$(2\pm 0.4)\times 10^{-11}$	10**	$(1\pm 0.2)\times 10^{12}$	$(2\pm 0.4)\times 10^{-11}$
NS	10**	$(4\pm 0.8)\times 10^{12}$	$(1\pm 0.2)\times 10^{-10}$	10**	$(3\pm 0.6)\times 10^{12}$	$(5\pm 1)\times 10^{-11}$
NS ⁺	10**	$(1\pm 0.2)\times 10^{11}$	$(3\pm 0.6)\times 10^{-12}$	10**	$(6\pm 1)\times 10^{10}$	$(1\pm 0.2)\times 10^{-12}$
DCS ⁺	10**	$<1.0\times 10^{11}$	$<3\times 10^{-12}$	10**	$<1.0\times 10^{11}$	$<2\times 10^{-12}$
CCCS	10**	$<3.2\times 10^{11}$	$<8\times 10^{-12}$	10**	$<3.2\times 10^{11}$	$<5\times 10^{-12}$

Notes. Abundances are computed assuming $N(\text{H}_2) = 1.9 \times 10^{22} \text{ cm}^{-2}$ towards the PDR and $N(\text{H}_2) = 2.9 \times 10^{22} \text{ cm}^{-2}$ towards the core from Gerin et al. (2009a). (*): computed including opacity effects. (**): since only one transition was detected, we assumed $T_{\text{rot}} = 10 \text{ K}$ and fitted the column density to match the observed T_{MB} assuming LTE.

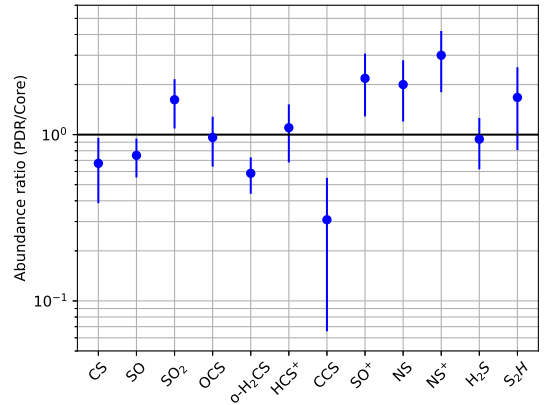
Table 2. Collisional partners and collisional excitation rates for the different species modelled with LVG.

Species	Collisional excitation rates
CS	Denis-Alpizar et al. (2013)
SO	Lique et al. (2006b)
SO ₂	Green (1995)
OCS	Green & Chapman (1978)
H ₂ CS	Wiesenfeld & Faure (2013)
HCS ⁺	Flower (1999)*

Notes. (*): Adapted from HCO⁺ collisional rates.

rates are available either in the range 10 to 50 K (Lique et al. 2006b) or 60 to 300 K (Lique et al. 2006a). For our simulations, we used the low temperature collisional rates from Lique et al. (2006b).

Histograms and density plots showing the results of the MCMC analysis are depicted in Fig. B.1. The kinetic temperatures and column densities thus derived are summarized in Table 4. Kinetic temperatures derived from RADEX are systematically higher than those derived from rotational diagrams, which is consistent with sub-thermal excitation. For most molecules, column densities derived from rotational diagrams and RADEX give compatible results, within uncertainties. However, some prominent exceptions are observed. In the PDR, beam-averaged column densities of CS and SO derived from rotational diagrams are two times larger than values derived using RADEX. In the core, the SO abundance derived from rotational diagrams is two times larger than the abundance obtained from RADEX. Since RADEX models take into account non-LTE effects, we consider results from RADEX models to be better constrained than those coming from rotational diagrams, and we adopt them in the following discussion. We note that, because of the effects of high optical depth, column densities derived using LTE should be lower than those obtained using RADEX. However, we have corrected LTE values for opacity effects (see Eq. 3). The opacity has


Fig. 3. Ratio between the abundance in the PDR/core position for each species.

been derived from the ratio of the integrated intensity of the main isotopologue over the less abundant one, assuming that T_{ex} is the same for all the isotopologues. An overestimation of the opacity would lead to an error in the column density calculation. In addition, the assumption of the same rotation temperature for all transitions used in LTE is not always accurate. In any case, the differences between LTE and RADEX models are within the uncertainties inherent to this kind of calculation.

6. Molecular abundances

To derive the abundances shown in Tables 1 and 4 we have assumed $N(\text{H}_2) = 1.9 \times 10^{22} \text{ cm}^{-2}$ at PDR and $N(\text{H}_2) = 2.9 \times 10^{22} \text{ cm}^{-2}$ at the core (Gerin et al. 2009a), and $N(\text{H}) = 0$ at both positions, meaning that gas is mostly molecular. Given the large beam sizes implied, we consider that this is a valid assumption for the PDR. The $N(\text{H}_2)$ values were

Table 3. Upper limits to the column density and abundance of undetected species.

Molecule	Freq (GHz)	rms ¹ (mK)	N _X ² (cm ⁻²)	Abundances wrt H ₂			Ref
				Horsehead	Dark clouds	Hot cores	
S ₂ H ₂	139.885	9	<8.5×10 ¹¹	<4.5×10 ⁻¹¹			
HSO	158.391	30	<1.5×10 ¹²	<7.9×10 ⁻¹¹			
HCS	161.128	30	<3.0×10 ¹³	<1.6×10 ⁻⁹	~1–5×10 ⁻¹⁰		Agúndez et al. (2018)
HSC	81.200	17	<7.5×10 ¹¹	<3.9×10 ⁻¹¹	~6×10 ⁻¹²		Agúndez et al. (2018)
HCCS	88.023	4	<3.6×10 ¹¹	<1.9×10 ⁻¹¹			
NCS	91.501	4	<7.0×10 ¹¹	<3.7×10 ⁻¹¹			
HNCS	82.102	8	<4.2×10 ¹¹	<2.2×10 ⁻¹¹	~4×10 ⁻¹²	~8×10 ⁻¹²	Adande et al. (2010)
HSCN	92.230	5	<4.0×10 ¹¹	<2.1×10 ⁻¹¹	~3.5×10 ⁻¹²	~2×10 ⁻¹²	Adande et al. (2010)
HCNS	86.118	8	<8.0×10 ¹⁰	<4.2×10 ⁻¹²			
HSNC	87.900	3	<8.0×10 ¹⁰	<4.2×10 ⁻¹²			
H ₂ C ₃ S	85.728	8	<8.0×10 ¹²	<4.2×10 ⁻¹⁰			
CH ₃ SH	99.185	7	<1.2×10 ¹³	<6.3×10 ⁻¹⁰		~4×10 ⁻⁹	Majumdar et al. (2016)
CS ⁺	103.933	7	<1.5×10 ¹²	<7.9×10 ⁻¹¹			
HSCO ⁺	90.183	4	<3.5×10 ¹¹	<1.8×10 ⁻¹¹			
HOCS ⁺	91.624	4	<3.5×10 ¹¹	<1.8×10 ⁻¹¹			
HOSO ⁺	88.452	4	<4.5×10 ¹¹	<1.8×10 ⁻¹¹			

Notes. (1) The rms has been calculated for a channel width of ≈ 0.33 km s⁻¹. The obtained rms is similar in the two surveyed positions. (2) 3σ upper limits assuming LTE, $T_{rot} = 10$ K, and a linewidth of 0.6 km s⁻¹. Abundances in the Horsehead were derived assuming $N(\text{H}_2) = 1.9 \times 10^{22}$ cm⁻²

Table 4. Mean values for kinetic temperatures, gas densities, column densities, and molecular abundances from RADEX models explored with MCMC.

Species	PDR				Core			
	T _K (K)	n _{H₂} (cm ⁻³)	N(X) (cm ⁻²)	Abundance $\frac{N(X)}{N(\text{H})+2N(\text{H}_2)}$	T _K (K)	n _{H₂} (cm ⁻³)	N(X) (cm ⁻²)	Abundance $\frac{N(X)}{N(\text{H})+2N(\text{H}_2)}$
CS	58±10	(5.3±1.7)×10 ⁴	(1.7±0.4)×10 ¹³	(4.5±1.1)×10 ⁻¹⁰	27±6	(9.5±3.2)×10 ⁴	(3.9±0.7)×10 ¹³	(6.7±1.2)×10 ⁻¹⁰
SO	44±12	(6.9±2.2)×10 ⁴	(1.5±0.2)×10 ¹³	(3.9±0.5)×10 ⁻¹⁰	15±3	(2.1±0.7)×10 ⁵	(3.0±0.4)×10 ¹³	(5.2±0.7)×10 ⁻¹⁰
SO ₂	58±10	(7.0±2.3)×10 ⁴	(4.4±0.8)×10 ¹²	(1.2±0.2)×10 ⁻¹⁰	25±8	(1.1±0.4)×10 ⁵	(4.3±0.7)×10 ¹²	(7.4±1.2)×10 ⁻¹¹
OCS	61±10	(7.5±3.7)×10 ⁴	(1.9±0.3)×10 ¹²	(5.0±0.8)×10 ⁻¹¹	24±6	(1.0±0.5)×10 ⁵	(3.0±0.5)×10 ¹²	(5.2±0.9)×10 ⁻¹¹
o-H ₂ CS	59±10	(5.0±1.7)×10 ⁴	(9.0±1.0)×10 ¹¹	(2.4±0.3)×10 ⁻¹¹	18±6	(9.1±3.4)×10 ⁴	(2.4±0.3)×10 ¹²	(4.1±0.5)×10 ⁻¹¹
p-H ₂ CS	–	–	–	–	22±6	(9.0±3.4)×10 ⁴	(9.0±2.0)×10 ¹¹	(1.6±0.4)×10 ⁻¹¹
HCS ⁺	54±10	(3.0±0.8)×10 ⁴	(4.1±0.8)×10 ¹¹	(1.1±0.2)×10 ⁻¹¹	–	–	–	–

Notes. Abundances are computed assuming $N(\text{H}_2) = 1.9 \times 10^{22}$ cm⁻² in the PDR and $N(\text{H}_2) = 2.9 \times 10^{22}$ cm⁻² (Gerin et al. 2009a).

derived using a beam of 12''. Following our assumption that the emission is extended and uniform, they should be the same with a larger beam of 25''. We assume this hypothesis to be coherent with our previous studies (Gerin et al. 2009b; Pety et al. 2012; Guzmán et al. 2014).

Our first result is that the fractional abundances and molecular abundance ratios estimated towards the two surveyed positions agree within a factor of approximately three. This gentle gradient is likely due to the limited angular resolution of our observations, which do not resolve the thin outer layers of the PDR. In fact, using interferometric observations, Goicoechea et al. (2006) derived CS abundances towards the outer PDR layers that are approximately five times larger than those presented in this study. Moreover, the line of sight towards the core also intersects the PDR layer in the cloud surface, which makes the detection of chemical gradients more difficult. A factor of two to three, however, can be significant given the high S/N ratio in our spectra and the peculiar observational strategy of WHISPER, which avoids calibration and pointing errors. The C- bearing species C₂S and o-H₂CS present frac-

tional abundances a factor of > two higher in the core than towards the PDR (see Fig 3). In contrast, the O-bearing molecules SO, SO₂, and OCS present similar abundances towards both positions. The same is true for the HCS⁺. Other species, S₂H, SO⁺, NS, and the recently discovered ion NS⁺, are more abundant towards the PDR than towards the core. This work identifies NS and NS⁺ as new PDR-like species.

We have unsuccessfully searched for the following sulphuretted compounds: CS⁺, HCS, HSC, HCCS, NCS, HNCS, HSCN, HCNS, HSNC, HSOC⁺, HOCS⁺, H₂C₃S, and CH₃SH. Some of them, HCS, HSC, HNCS, HSCN, and CH₃SH, were previously detected in the interstellar medium. The radicals HCS and HSC were recently detected towards the dark cloud L483, with abundances of a few 10⁻¹⁰ and various 10⁻¹² respectively (Agúndez et al. 2018). HNCS and HSCN were detected in the envelope of Sgr B2 and towards TMC 1 (Adande et al. 2010). The organic sulphur compound CH₃SH has been detected in hot cores (Sgr B2: Linke et al. 1979, G327.3-0.6: Gibb et al. 2000; Orion: Kolesníková et al. 2014). Majumdar et al.

and in diffuse clouds was observed toward several Galactic sight lines by Godard et al. (2012), who showed that turbulent dissipation and shocks provide the required energy to form SH^+ in these very low density clouds. To our knowledge, SH^+ has not been detected in the Horsehead. This is not surprising since this ion is hardly formed in this nebula. In PDRs, $\text{H}_2(v=2)$ and higher vibrational levels are mostly populated by FUV pumping. Since the FUV flux in the Horsehead is not strong, the layer where $\text{H}_2(v=2)$ is excited is most likely very narrow, thus strongly diluted to be detected with single-dish telescopes.

Other routes to the formation of NS^+ involve the ionic species H_2S^+ and S^+ . Because of its low ionization potential, sulfur is expected to be ionized up to $A_v \sim 7$ mag (see e.g. Le Gal et al. 2017) and is a plausible precursor of NS^+ . The abundance of the ion H_2S^+ , formed by the reaction $\text{S} + \text{H}_3^+$, might be important in deeper layers of the molecular cloud depending on the cosmic ray ionization rate (Sternberg & Dalgarno 1995).

Within this scenario, NS^+ could be considered as a PDR tracer. This ion has been widely detected in the interstellar medium (Cernicharo et al. 2018). One possibility is that NS^+ emission is coming from the UV-illuminated external layers of the cloud. To check this hypothesis, in Fig. 5 we represent the NS^+ abundance as a function of the total H_2 column density for all the reported NS^+ detections thus far. The NS^+ abundance is anti-correlated with $N(\text{H}_2)$, as expected if the NS^+ emission is coming mainly from the cloud surface.

The chemistry of NS is poorly understood as well. This compound is detected in very different environments such as dark clouds and hot cores (Fuente et al. 2016; Cernicharo et al. 2018) as well as towards the Orion Bar (Leurini et al. 2006). Moreover, NS has been detected in comets with an abundance of 0.006-0.12 % relative to water (Calmonte et al. 2016). Ice evaporation might be the origin of NS in hot cores (Vidal et al. 2017; Viti et al. 2004). Other desorption mechanisms (photodesorption, cosmic-rays, grain sputtering) might release some NS molecules to the gas phase even in cold environments. We recall that Fuente et al. (2017) also proposed that these desorption processes would release H_2S and S_2H molecules from the grain surfaces, boosting their abundances in gas phase.

7.2. Sulphur budget in the Horsehead

The main reservoir of sulphur in gas phase is still debated. In dark cores, only about 0.05% is locked in the S-bearing molecules detected at millimeter wavelengths (see the fractional abundances derived for S-bearing species towards the dark cloud TMC1-CP in Table 5). Unfortunately, most of the plausible major sulphur reservoirs such as S, HS, and S_2 are either not observable or very difficult to observe at millimeter wavelengths and one needs to trust to chemical models to estimate the exact amount of sulphur in the gas phase. It is widely accepted that most of the sulphur is locked in icy grain mantles. This is corroborated by the observations of S-bearing species in comets. In a recent compilation, Bockelée-Morvan & Biver (2017) estimated that the S/O elemental ratio in the comet ice is about 1.5 %, which is consistent within a factor of approximately four with the solar value, H_2S being the main sulphur reservoir. Hot cores are compact warm regions where the icy mantles evaporate releasing the sulphur budget to the gas. Orion

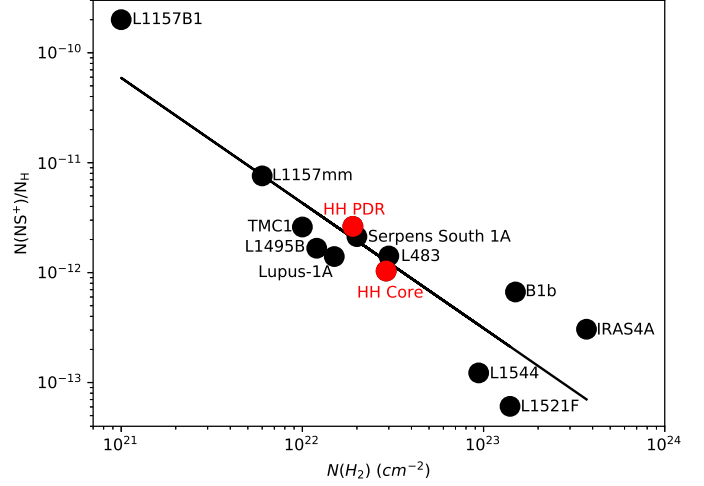


Fig. 5. Abundances of NS^+ as a function of $N(\text{H}_2)$. Black points corresponds to the detections reported by Cernicharo et al. (2018). Red points corresponds to the core and PDR positions in the Horsehead. The black solid line depicts a linear fit to the data.

KL is the best-studied hot core, with full spectral surveys at millimeter and submillimeter wavelengths. In Table 5, we show the abundances of sulphur species that have been derived in this prototypical hot core. Gas phase H_2S is the main sulphur reservoir in this hot core and the elemental gas-phase sulphur abundance is $\sim 1.6 \times 10^{-6}$ (Crockett et al. 2014). Fuente et al. (2019) obtained a similar value for the sulphur gas phase abundance of $\sim 10^{-6}$ in the edges of the TMC1 molecular cloud.

Based on the WHISPER survey, we have determined a significant inventory of sulphur species and their abundances in the Horsehead PDR. Only one H_2S line has been observed and the estimated value of the H_2S abundance ($\sim 0.3 - 5 \times 10^{-9}$) is hence uncertain. It seems clear, however, that the abundance of gaseous H_2S is far from that observed in Orion-KL. One possibility is that a large fraction of H_2S remains in the solid state. This is expected since the dust temperature in this PDR is around $\sim 20-30$ K in the PDR (Goicoechea et al. 2009), which is below the sublimation temperature of H_2S , ~ 80 K (Jiménez-Escobar & Muñoz Caro 2011). The detections of SO^+ and NS^+ suggest that a significant fraction of sulphur is in the form of S^+ in the outer layers of this cloud. Sulphur chemistry is still poorly known, and especially surface chemistry reactions need further understanding. Oba et al. (2018) demonstrated that chemical desorption is an efficient mechanism for sulphur-bearing-molecule formation at least in some cases, such as H_2S . Given the high fraction of sulphur present in a solid state ($\sim 90\%$), their work highlights the importance of chemical desorption for understanding the abundances of the different molecular species in the gaseous phase.

Although it has been widely debated what the main sulphur reservoirs in the interstellar medium are, little information is available about the sulphur chemistry in PDRs thus far. Our study shows that CS, SO, and H_2S are the most abundant observable S-bearing molecules in the Horsehead PDR, with similar abundances within one or-

Table 5. Comparison of fractional abundances with observational templates.

	HH-PDR	TMC 1-CP	Orion KL	Comets (% wrt H ₂ O)
CS	$(4.5\pm 1.1)\times 10^{-10}$	1.4×10^{-9}	7.0×10^{-8}	0.02–0.2
SO	$(3.9\pm 0.5)\times 10^{-10}$	7.5×10^{-10}	8.0×10^{-8}	0.04–0.3
o-H ₂ CS	$(2.4\pm 0.3)\times 10^{-11}$	3.0×10^{-10}	5.6×10^{-9}	0.009–0.09
OCS	$(5.0\pm 0.8)\times 10^{-11}$	1.1×10^{-9}	5.0×10^{-8}	0.03–0.4
CCS	$(8.0\pm 2.6)\times 10^{-12}$	3.5×10^{-9}	8.0×10^{-11}	
SO ₂	$(1.2\pm 0.2)\times 10^{-10}$	1.5×10^{-10}	1.9×10^{-7}	0.2
SO ⁺	$(1.7\pm 0.5)\times 10^{-11}$			
HCS ⁺	$(1.1\pm 0.2)\times 10^{-11}$	1.5×10^{-10}		
NS	$(1.0\pm 0.2)\times 10^{-10}$	4.0×10^{-10}	3.4×10^{-9}	0.006–0.012
NS ⁺	$(3.0\pm 0.6)\times 10^{-12}$	2.4×10^{-12}		
H ₂ S	$(3.1\pm 0.5)\times 10^{-10}$	$<2.5\times 10^{-10}$	1.5×10^{-6}	0.13–1.5
S ₂ H	$(8.7\pm 3.1)\times 10^{-11}$			
sulphur budget	$\sim 1.5\times 10^{-9}$	$\sim 8\times 10^{-9}$	1.9×10^{-6}	4×10^{-6} (n(H ₂ O)/n _H = 2.7×10^{-4})

Notes. Refs: TMC1: Agúndez & Wakelam (2013); Cernicharo et al. (2018) and references therein; Orion-KL: Tercero et al. (2010); Esplugues et al. (2014); Crockett et al. (2014); Comets: Calmonte et al. (2016); Bockelée-Morvan & Biver (2017).

der of magnitude. The total abundance of S atoms locked in these three species is \sim a few 10^{-9} , only $\sim 0.1\%$ of the total number of atoms. Therefore, they do not constitute the main sulphur reservoir. An important fraction of sulphur atoms might be forming icy mantles in these low-UV irradiated regions. Dust grain temperatures in this low-UV PDR are ~ 20 – 30 K, lower than the evaporation temperature of H₂S, the main sulphur reservoir in solid state. In the gas phase, S and S⁺ are expected to be the main sulphur reservoirs (Le Gal et al. 2017; Goicoechea et al. 2006). Unfortunately the observation of these species is not easy in the (sub-)millimeter wavelength range. Although weak and difficult to interpret, the detection of a sulphur recombination line by Roshi et al. (2014) in NGC 2024 provides evidence for large abundances of S and S⁺ in the gas phase.

8. Conclusions

Photodissociation regions constitute the transition between diffuse clouds, in which sulphur is mainly in the gaseous phase, and cold cores where S-bearing molecules are heavily depleted; therefore they are essential regions to understand sulphur chemistry. Here we present a complete inventory of S-bearing molecules and their abundances in the Horsehead nebula based on the WHISPER survey. Two positions are targeted in this survey, one coincident with a dense core and the other at the PDR-line species peak (PDR). The detections towards the PDR are especially interesting since this is the most complete observational study of S-bearing species in a PDR thus far.

We have detected 13 S-bearing species (CS, SO, SO₂, OCS, H₂CS – both ortho and para – HDCS, C₂S, HCS⁺, SO⁺, H₂S, S₂H, NS, and NS⁺) towards the PDR and core positions in the Horsehead nebula.

Two prominent results of this study are the detection of SO⁺ and NS⁺ for the first time in a PDR. Comparing the core and PDR positions, we find a differentiated chemical behaviour between C-S and O-S bearing species. The C-S bearing species C₂S and o-H₂CS present fractional abundances a factor of $>$ two higher in the core than in the PDR. In contrast, the O-S bearing molecules SO, SO₂, and OCS present similar abundances towards both positions. The same is true for the HCS⁺. A few molecules are

more abundant towards the PDR than towards the core: S₂H, SO⁺, NS, and NS⁺. Fuente et al. (2017) proposed S₂H to be a good tracer of low-UV PDRs, where an active grain surface chemistry and gaseous photo-chemistry coexist. We are aware that, with our limited angular resolution, it is doubtful to conclude that NS⁺ is mainly coming from the PDR. Yet NS⁺ behaves like other S-bearing molecules that have been interpreted as UV tracers, such as SO⁺ and S₂H. Therefore it is worth investigating the link between the enhanced UV-field in PDRs and NS⁺ abundances.

Acknowledgements. We thank the Spanish MINECO for funding support from AYA2016-75066-C2-1/2-P, AYA2017-85111-P and ERC under ERC-2013-SyG, G. A. 610256 NANOCOSMOS. JRG thanks the Spanish MCIU for funding support under grant AYA2017-85111-P. This work was supported by the Programme National “Physique et Chimie du Milieu Interstellaire” (PCMI) of CNRS/INSU with INC/INP co-funded by CEA and CNES.

References

- Adande, G. R., Halfen, D. T., Ziurys, L. M., Quan, D., & Herbst, E. 2010, *ApJ*, 725, 561
- Agúndez, M., Marcelino, N., Cernicharo, J., & Tafalla, M. 2018, *A&A*, 611, L1
- Agúndez, M. & Wakelam, V. 2013, *Chemical Reviews*, 113, 8710
- Asplund, M., Grevesse, N., & Sauval, A. J. 2005, in *Astronomical Society of the Pacific Conference Series*, Vol. 336, *Cosmic Abundances as Records of Stellar Evolution and Nucleosynthesis*, ed. T. G. Barnes, III & F. N. Bash, 25
- Benz, A. O., Bruderer, S., van Dishoeck, E. F., et al. 2010, *A&A*, 521, L35
- Bockelée-Morvan, D. & Biver, N. 2017, *Philosophical Transactions of the Royal Society of London Series A*, 375, 20160252
- Boogert, A. C. A., Schutte, W. A., Helmich, F. P., Tielens, A. G. G. M., & Wooden, D. H. 1997, *A&A*, 317, 929
- Calmonte, U., Altwegg, K., Balsiger, H., et al. 2016, *MNRAS*, 462, S253
- Cernicharo, J., Lefloch, B., Agúndez, M., et al. 2018, *ApJ*, 853, L22
- Crockett, N. R., Bergin, E. A., Neill, J. L., et al. 2014, *ApJ*, 787, 112
- Cuadrado, S., Goicoechea, J. R., Cernicharo, J., et al. 2017, *A&A*, 603, A124
- Cuadrado, S., Goicoechea, J. R., Pilleri, P., et al. 2015, *A&A*, 575, A82
- Denis-Alpizar, O., Stoecklin, T., Halvick, P., & Dubernet, M.-L. 2013, *The Journal of Chemical Physics*, 139, 204304
- Draine, B. T. 1978, *ApJS*, 36, 595
- Esplugues, G. B., Viti, S., Goicoechea, J. R., & Cernicharo, J. 2014, *A&A*, 567, A95
- Flower, D. R. 1999, *MNRAS*, 305, 651

- Foreman-Mackey, D., Hogg, D. W., Lang, D., & Goodman, J. 2012
- Fuente, A., Cernicharo, J., Roueff, E., et al. 2016, *A&A*, 593, A94
- Fuente, A., Goicoechea, J. R., Pety, J., et al. 2017, *ApJ*, 851, L49
- Fuente, A., Martin-Pintado, J., Cernicharo, J., & Bachiller, R. 1993, *A&A*, 276, 473
- Fuente, A., Martin-Pintado, J., Neri, R., Rogers, C., & Moriarty-Schieven, G. 1996, *A&A*, 310, 286
- Fuente, A., Martin-Pintado, J., Rodriguez-Fernández, N. J., Cernicharo, J., & Gerin, M. 2000, *A&A*, 354, 1053
- Fuente, A., Navarro, D. G., Caselli, P., et al. 2019, *A&A*, 624, A105
- Fuente, A., Rodriguez-Franco, A., Garcia-Burillo, S., Martin-Pintado, J., & Black, J. H. 2003, *A&A*, 406, 899
- Geballe, T. R., Baas, F., Greenberg, J. M., & Schutte, W. 1985, *A&A*, 146, L6
- Gerin, M., Goicoechea, J. R., Pety, J., & Hily-Blant, P. 2009a, *A&A*, 494, 977
- Gerin, M., Pety, J., & Goicoechea, J. R. 2009b, in *Astronomical Society of the Pacific Conference Series*, Vol. 417, *Submillimeter Astrophysics and Technology: a Symposium Honoring Thomas G. Phillips*, ed. D. C. Lis, J. E. Vaillancourt, P. F. Goldsmith, T. A. Bell, N. Z. Scoville, & J. Zmuidzinas, 165
- Gibb, E., Nummelin, A., Irvine, W. M., Whittet, D. C. B., & Bergman, P. 2000, *ApJ*, 545, 309
- Ginard, D., González-García, M., Fuente, A., et al. 2012, *A&A*, 543, A27
- Godard, B., Falgarone, E., Gerin, M., et al. 2012, *A&A*, 540, A87
- Goicoechea, J. R., Compiègne, M., & Habart, E. 2009, *ApJ*, 699, L165
- Goicoechea, J. R., Cuadrado, S., Pety, J., et al. 2017, *A&A*, 601, L9
- Goicoechea, J. R., Pety, J., Cuadrado, S., et al. 2016, *Nature*, 537, 207
- Goicoechea, J. R., Pety, J., Gerin, M., et al. 2006, *A&A*, 456, 565
- Goldsmith, P. F. & Langer, W. D. 1999, *ApJ*, 517, 209
- Goodman, J. & Weare, J. 2010, *Communications in Applied Mathematics and Computational Science*, Vol. 5, No. 1, p. 65-80, 2010, 5, 65
- Gratier, P., Pety, J., Guzmán, V., et al. 2013, *A&A*, 557, A101
- Green, S. 1995, *ApJS*, 100, 213
- Green, S. & Chapman, S. 1978, *ApJS*, 37, 169
- Guzmán, V., Pety, J., Goicoechea, J. R., Gerin, M., & Roueff, E. 2011, *A&A*, 534, A49
- Guzmán, V., Pety, J., Gratier, P., et al. 2012, *A&A*, 543, L1
- Guzmán, V. V., Goicoechea, J. R., Pety, J., et al. 2013, *A&A*, 560, A73
- Guzmán, V. V., Pety, J., Goicoechea, J. R., et al. 2015, *ApJ*, 800, L33
- Guzmán, V. V., Pety, J., Gratier, P., et al. 2014, *Faraday Discussions*, 168, 103
- Habart, E., Abergel, A., Walmsley, C. M., Teyssier, D., & Pety, J. 2005, *A&A*, 437, 177
- Jiménez-Escobar, A. & Muñoz Caro, G. M. 2011, *A&A*, 536, A91
- Jiménez-Escobar, A., Muñoz Caro, G. M., & Chen, Y.-J. 2014, *MNRAS*, 443, 343
- Kolesniková, L., Tercero, B., Cernicharo, J., et al. 2014, *ApJ*, 784, L7
- Le Gal, R., Herbst, E., Dufour, G., et al. 2017, *A&A*, 605, A88
- Leurini, S., Rolfs, R., Thorwirth, S., et al. 2006, *A&A*, 454, L47
- Linke, R. A., Frerking, M. A., & Thaddeus, P. 1979, *ApJ*, 234, L139
- Lique, F., Dubernet, M.-L., Spielfeldel, A., & Feautrier, N. 2006a, *A&A*, 450, 399
- Lique, F., Spielfeldel, A., & Cernicharo, J. 2006b, *A&A*, 451, 1125
- Majumdar, L., Gratier, P., Vidal, T., et al. 2016, *MNRAS*, 458, 1859
- Marcelino, N., Cernicharo, J., Roueff, E., Gerin, M., & Mauersberger, R. 2005, *ApJ*, 620, 308
- Menten, K. M., Wyrowski, F., Belloche, A., et al. 2011, *A&A*, 525, A77
- Minissale, M., Dulieu, F., Cazaux, S., & Hocuk, S. 2016, *A&A*, 585, A24
- Müller, H. S. P., Goicoechea, J. R., Cernicharo, J., et al. 2014, *A&A*, 569, L5
- Nagy, Z., Van der Tak, F. F. S., Ossenkopf, V., et al. 2013, *A&A*, 550, A96
- Neufeld, D. A., Godard, B., Gerin, M., et al. 2015, *A&A*, 577, A49
- Oba, Y., Tomaru, T., Lamberts, T., Kouchi, A., & Watanabe, N. 2018, *Nature Astronomy*, 2, 228
- Palumbo, M. E., Tielens, A. G. G. M., & Tokunaga, A. T. 1995, *ApJ*, 449, 674
- Penzias, A. A. & Burrus, C. A. 1973, *ARA&A*, 11, 51
- Pety, J., Goicoechea, J. R., Hily-Blant, P., Gerin, M., & Teyssier, D. 2007, *A&A*, 464, L41
- Pety, J., Gratier, P., Guzmán, V., et al. 2012, *A&A*, 548, A68
- Pety, J., Teyssier, D., Fossé, D., et al. 2005, *A&A*, 435, 885
- Pillari, P., Fuente, A., Cernicharo, J., et al. 2012, *A&A*, 544, A110
- Pillari, P., Fuente, A., Gerin, M., et al. 2014, *A&A*, 561, A69
- Pillari, P., Treviño-Morales, S., Fuente, A., et al. 2013, *A&A*, 554, A87
- Roshi, D. A., Goss, W. M., & Jeyakumar, S. 2014, *ApJ*, 793, 83
- Sternberg, A. & Dalgarno, A. 1995, *ApJS*, 99, 565
- Tercero, B., Cernicharo, J., Pardo, J. R., & Goicoechea, J. R. 2010, *A&A*, 517, A96
- Tieftrunk, A., Pineau des Forets, G., Schilke, P., & Walmsley, C. M. 1994, *A&A*, 289, 579
- Treviño-Morales, S. P., Fuente, A., Sánchez-Monge, Á., et al. 2016, *A&A*, 593, L12
- Treviño-Morales, S. P., Pillari, P., Fuente, A., et al. 2014, *A&A*, 569, A19
- Turner, B. E. 1992, *ApJ*, 396, L107
- Turner, B. E. 1994, *ApJ*, 430, 727
- Turner, B. E. 1996, *ApJ*, 468, 694
- van der Tak, F. F. S., Black, J. H., Schöier, F. L., Jansen, D. J., & van Dishoeck, E. F. 2007, *A&A*, 468, 627
- Vastel, C., Quénard, D., Le Gal, R., et al. 2018, *MNRAS*, 478, 5514
- Vidal, T. H. G., Loison, J.-C., Jaziri, A. Y., et al. 2017, *MNRAS*, 469, 435
- Viti, S., Collings, M. P., Dever, J. W., McCoustra, M. R. S., & Williams, D. A. 2004, *MNRAS*, 354, 1141
- Wakelam, V., Caselli, P., Ceccarelli, C., Herbst, E., & Castets, A. 2004, *A&A*, 422, 159
- Wiesenfeld, L. & Faure, A. 2013, *MNRAS*, 432, 2573
- Wilson, T. L. & Rood, R. 1994, *ARA&A*, 32, 191
- Zanchet, A., Agúndez, M., Herrero, V. J., Aguado, A., & Roncero, O. 2013, *AJ*, 146, 125
- Zanchet, A., Lique, F., Roncero, O., Goicoechea, J. R., & Bulut, N. 2019, *arXiv e-prints*, arXiv:1905.02779

Appendix A: Tables and figures

Appendix B: Distribution of model parameters from MCMC simulations

Table A.1. Gaussian fits to the IRAM 30m lines.

		PDR				Core			
		T_{MB} (K)	v_{LSR} (km s ⁻¹)	Δv	$\int T_{MB} dv$ (K km s ⁻¹)	T_{MB} (K)	v_{LSR} (km s ⁻¹)	Δv	$\int T_{MB} dv$ (K km s ⁻¹)
CS	2→1	3.00	10.70±0.01	0.76±0.01	2.440±0.003	5.60	10.67±0.01	0.79±0.01	4.752±0.004
	3→2	2.20	10.67±0.01	0.74±0.01	1.705±0.009	4.70	10.63±0.01	0.74±0.01	3.662±0.007
	5→4	0.94	10.65±0.01	0.59±0.01	0.592±0.007	1.20	10.61±0.01	0.63±0.01	0.805±0.007
C ³⁴ S	2→1	0.41	10.72±0.01	0.55±0.01	0.241±0.003	0.78	10.70±0.01	0.61±0.01	0.505±0.002
	3→2	0.34	10.72±0.01	0.54±0.03	0.195±0.008	0.49	10.67±0.01	0.56±0.01	0.291±0.007
	5→4	0.05	10.57±0.06	0.46±0.12	0.027±0.006	-	-	-	-
¹³ CS	2→1	0.11	10.71±0.01	0.52±0.03	0.063±0.003	0.20	10.70±0.01	0.58±0.02	0.127±0.003
	3→2	0.05	10.61±0.07	0.66±0.16	0.037±0.008	0.16	10.62±0.01	0.51±0.04	0.088±0.006
C ³³ S	2→1	0.07	11.50±0.02	0.48±0.05	0.034±0.003	0.09	11.46±0.02	0.74±0.05	0.074±0.004
	3→2	-	-	-	-	0.08	10.92±0.05	0.56±0.09	0.046±0.007
CCS	6 ₇ →5 ₆	0.09	10.76±0.04	0.42±0.09	0.042±0.008	0.31	10.70±0.01	0.44±0.03	0.146±0.007
	7 ₆ →6 ₅	0.04	10.76±0.03	0.35±0.06	0.014±0.002	0.09	10.70±0.01	0.37±0.04	0.037±0.003
	7 ₇ →6 ₆	0.04	10.73±0.03	0.40±0.07	0.017±0.003	0.08	10.68±0.01	0.47±0.03	0.042±0.002
	7 ₈ →6 ₇	0.07	10.71±0.02	0.48±0.03	0.036±0.002	0.23	10.69±0.01	0.47±0.01	0.117±0.002
	8 ₇ →7 ₆	-	-	-	-	0.08	10.76±0.02	0.33±0.05	0.030±0.003
	8 ₈ →7 ₇	0.04	10.74±0.03	0.32±0.08	0.013±0.002	0.07	10.68±0.02	0.39±0.05	0.031±0.003
OCS	7→6	0.02	10.72±0.06	0.57±0.11	0.014±0.003	0.06	10.69±0.04	0.75±0.09	0.045±0.005
	8→7	0.04	10.76±0.02	0.40±0.04	0.019±0.002	0.05	10.62±0.02	0.61±0.05	0.033±0.002
	9→8	0.05	10.66±0.05	0.48±0.14	0.024±0.005	0.07	10.76±0.03	0.45±0.01	0.034±0.004
	11→10	-	-	-	-	0.05	10.60±0.04	0.41±0.09	0.023±0.004
	12→11	-	-	-	-	0.08	10.50±0.05	0.59±0.14	0.048±0.009
p-H ₂ CS	3 ₀₃ →2 ₀₂	0.08	10.72±0.02	0.52±0.04	0.046±0.003	0.23	10.65±0.01	0.55±0.02	0.137±0.003
	4 ₀₄ →3 ₀₃	0.05	10.78±0.03	0.30±0.08	0.017±0.004	0.23	10.68±0.02	0.46±0.03	0.113±0.005
	6 ₀₆ →5 ₀₅	-	-	-	-	0.04	10.76±0.05	0.70±0.11	0.032±0.005
o-H ₂ CS	3 ₁₃ →2 ₁₂	0.13	10.68±0.01	0.47±0.03	0.066±0.003	0.33	10.65±0.01	0.51±0.01	0.179±0.003
	3 ₁₂ →2 ₁₁	0.14	10.75±0.05	0.47±0.03	0.071±0.003	0.30	10.71±0.01	0.55±0.01	0.177±0.003
	4 ₁₄ →3 ₁₃	0.16	10.65±0.02	0.49±0.04	0.084±0.005	0.31	10.61±0.01	0.52±0.02	0.173±0.005
	4 ₁₃ →3 ₁₂	0.10	10.84±0.02	0.44±0.05	0.046±0.005	0.28	10.80±0.02	0.43±0.02	0.131±0.005
HDCS	3 ₀₃ →2 ₀₂	-	-	-	-	0.06	10.63±0.02	0.34±0.04	0.022±0.002
	3 ₁₃ →2 ₁₂	-	-	-	-	-	-	-	-
	3 ₁₂ →2 ₁₁	0.05	10.79±0.02	0.31±0.05	0.018±0.002	0.05	10.79±0.02	0.50±0.08	0.027±0.003
HCS ⁺	2→1	0.13	10.75±0.02	0.73±0.03	0.102±0.004	0.11	10.75±0.01	0.66±0.03	0.073±0.003
	5→4	0.11	10.75±0.03	0.62±0.07	0.069±0.007	-	-	-	-
	6→5	0.06	10.64±0.05	0.65±0.14	0.039±0.006	-	-	-	-
SO	2 ₂ →1 ₁	0.45	10.72±0.01	0.50±0.01	0.241±0.005	0.50	10.66±0.01	0.55±0.08	0.293±0.003
	2 ₃ →1 ₂	3.20	10.73±0.01	0.58±0.01	2.004±0.003	4.50	10.66±0.01	0.65±0.01	3.151±0.003
	3 ₂ →2 ₁	0.55	10.73±0.01	0.48±0.01	0.285±0.004	0.73	10.64±0.01	0.50±0.01	0.392±0.005
	3 ₃ →2 ₂	0.70	10.72±0.01	0.43±0.01	0.317±0.005	1.10	10.61±0.01	0.45±0.01	0.521±0.005
	3 ₄ →2 ₃	2.40	10.68±0.01	0.56±0.01	1.466±0.005	4.40	10.61±0.01	0.58±0.01	2.731±0.007
	4 ₃ →3 ₂	0.55	10.69±0.01	0.52±0.02	0.305±0.011	0.92	10.60±0.01	0.45±0.02	0.442±0.013
	5 ₄ →4 ₃	0.34	10.69±0.01	0.63±0.01	0.225±0.003	0.40	10.61±0.01	0.59±0.02	0.254±0.007
	5 ₅ →4 ₄	0.34	10.70±0.01	0.45±0.01	0.166±0.007	0.40	10.59±0.01	0.48±0.02	0.204±0.007
	5 ₆ →4 ₅	1.23	10.68±0.01	0.62±0.01	0.812±0.007	1.48	10.62±0.01	0.60±0.01	0.944±0.006
³⁴ SO	2 ₂ →1 ₁	-	-	-	-	0.02	10.82±0.06	0.99±0.12	0.022±0.002
	2 ₃ →1 ₂	0.22	10.74±0.01	0.54±0.02	0.130±0.003	0.30	10.65±0.01	0.54±0.02	0.172±0.003
	3 ₂ →2 ₁	-	-	-	-	0.06	10.56±0.03	0.38±0.07	0.024±0.004
	3 ₄ →2 ₃	0.22	10.71±0.01	0.46±0.03	0.106±0.005	0.31	10.59±0.03	0.49±0.02	0.164±0.006
	5 ₆ →4 ₅	0.10	10.64±0.03	0.40±0.11	0.043±0.007	0.07	10.50±0.06	0.97±0.14	0.069±0.008
S ¹⁸ O	2 ₃ →1 ₂	-	-	-	-	0.04	10.67±0.04	0.66±0.09	0.028±0.003
SO ⁺	9/2→7/2 (e)	0.10	10.70±0.04	0.77±0.10	0.082±0.009	0.07	10.66±0.05	0.70±0.10	0.050±0.006
	9/2→7/2 (f)	0.09	10.73±0.03	0.67±0.07	0.068±0.006	0.05	10.77±0.11	0.96±0.30	0.047 ±0.011
	11/2→9/2 (e)	0.07	10.69±0.04	0.50±0.08	0.037±0.006	0.05	10.78±0.07	0.48±0.16	0.023±0.006
	11/2→9/2 (f)	0.05	10.72±0.05	0.67±0.12	0.037±0.005	-	-	-	-
SO ₂	3 ₁₃ →2 ₀₂	0.29	10.74±0.01	0.47±0.02	0.143±0.003	0.25	10.65±0.01	0.58±0.01	0.156±0.002
	5 ₁₅ →4 ₀₄	0.27	10.72±0.01	0.47±0.03	0.132±0.005	0.28	10.62±0.01	0.48±0.02	0.148±0.004
	3 ₂₂ →2 ₁₁	0.09	10.70±0.06	0.36±0.30	0.033±0.007	0.09	10.73±0.04	0.68±0.08	0.068±0.007
	4 ₂₂ →3 ₁₃	0.09	10.70±0.03	0.58±0.06	0.054±0.005	0.06	10.50±0.05	0.815±0.153	0.049±0.007
	5 ₂₄ →4 ₁₃	-	-	-	-	0.08	10.69±0.05	0.46±0.11	0.039±0.008
NS	5/2,7/2→3/2,5/2 (e)	0.18	10.77±0.04	0.61±0.08	0.12±0.01	0.20	10.91±0.03	0.54±0.05	0.110±0.010
	5/2,5/2→3/2,3/2 (e)	0.14	10.90±0.04	0.51±0.10	0.075±0.012	0.11	10.83±0.06	0.53±0.21	0.059±0.015
	5/2,3/2→3/2,1/2 (e)	0.12	11.07±0.04	0.59±0.09	0.074±0.010	0.10	10.84±0.06	0.58±0.22	0.063±0.015
	5/2,7/2→3/2,5/2 (f)	0.24	10.50±0.02	0.37±0.05	0.094±0.012	0.20	10.34±0.04	0.59±0.11	0.127±0.018
	5/2,5/2→3/2,3/2 (f)	0.14	10.58±0.07	0.56±0.22	0.084±0.024	0.16	10.38±0.04	0.27±0.12	0.045±0.014
	5/2,3/2→3/2,1/2 (f)	0.21	10.52±0.03	0.31±0.06	0.069±0.012	0.14	10.39±0.06	0.45±0.16	0.017±0.019
NS ⁺	2→1	0.034	10.46±0.04	0.77±0.08	0.028±0.002	0.017	10.44±0.09	1.0±0.3	0.019±0.004
	3→2	0.035	10.64±0.10	0.76±0.26	0.028±0.007	-	-	-	-

Notes. Tabulated errors are the numerical errors of the Gaussian fitting. Other kinds of errors such as calibration or pointing errors are not considered.

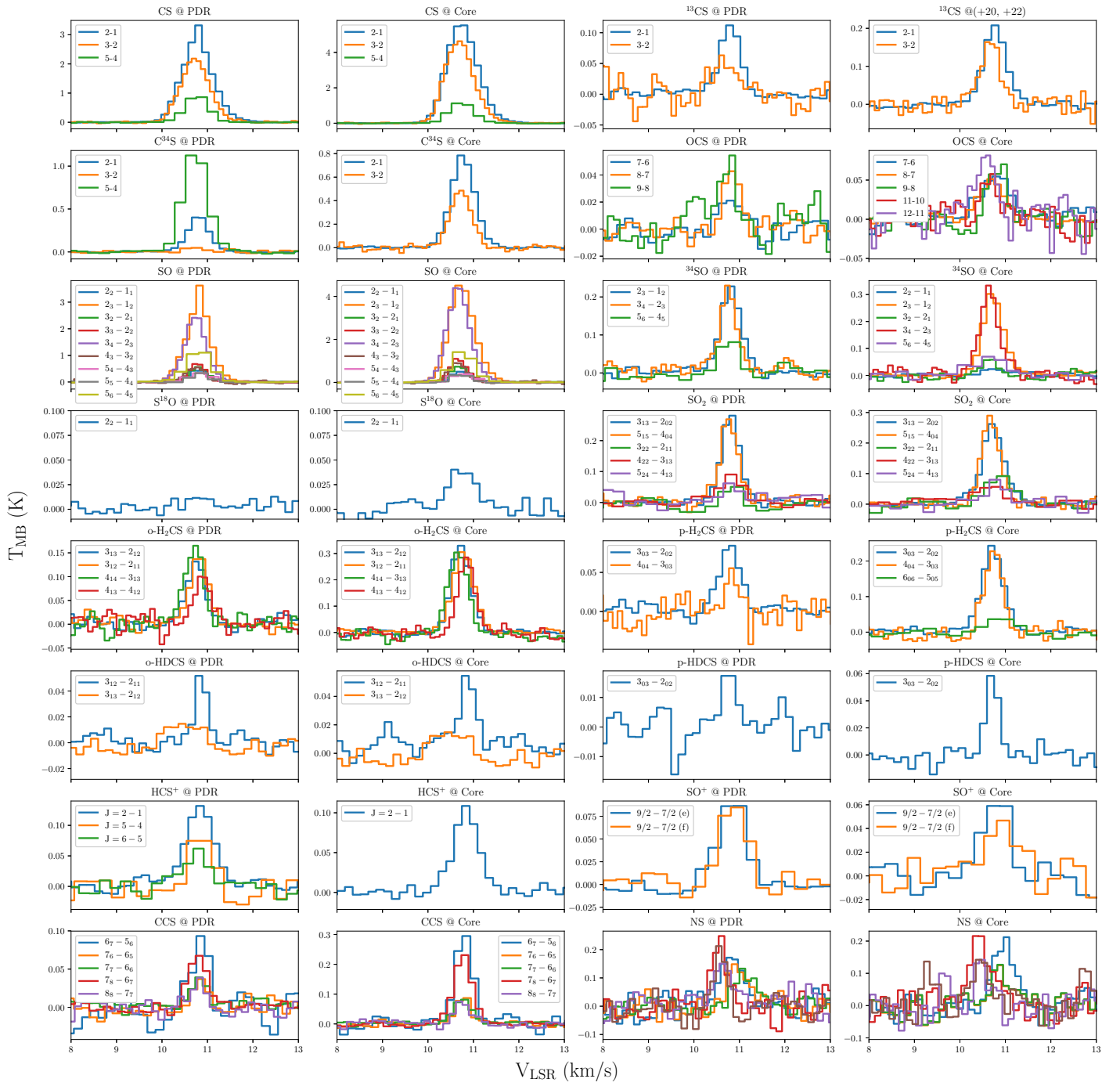


Fig. A.1. Detected species in the Horsehead.

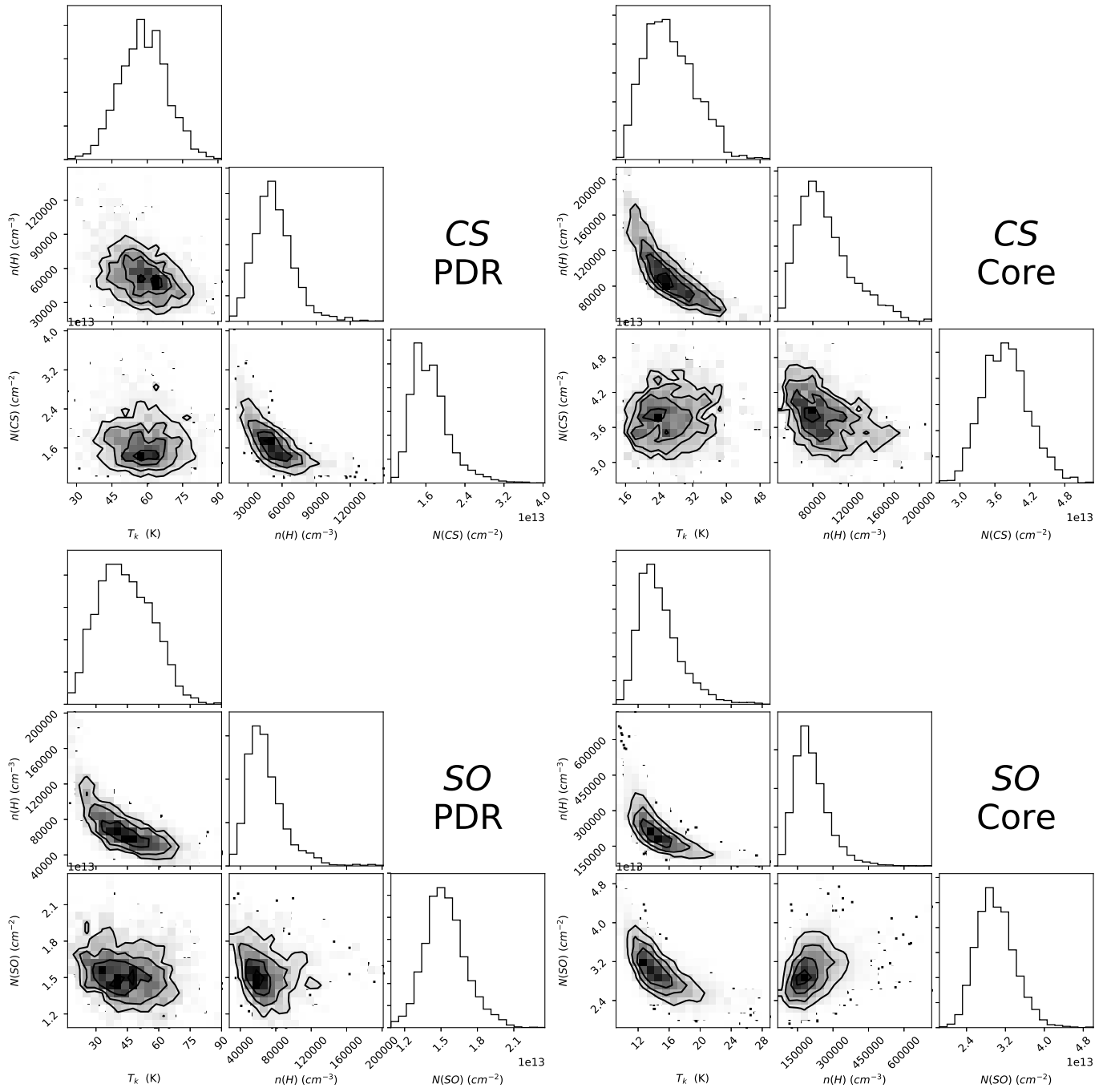


Fig. B.1. Histograms of the MCMC RADEX parameter distribution for the different molecules and regions studied.

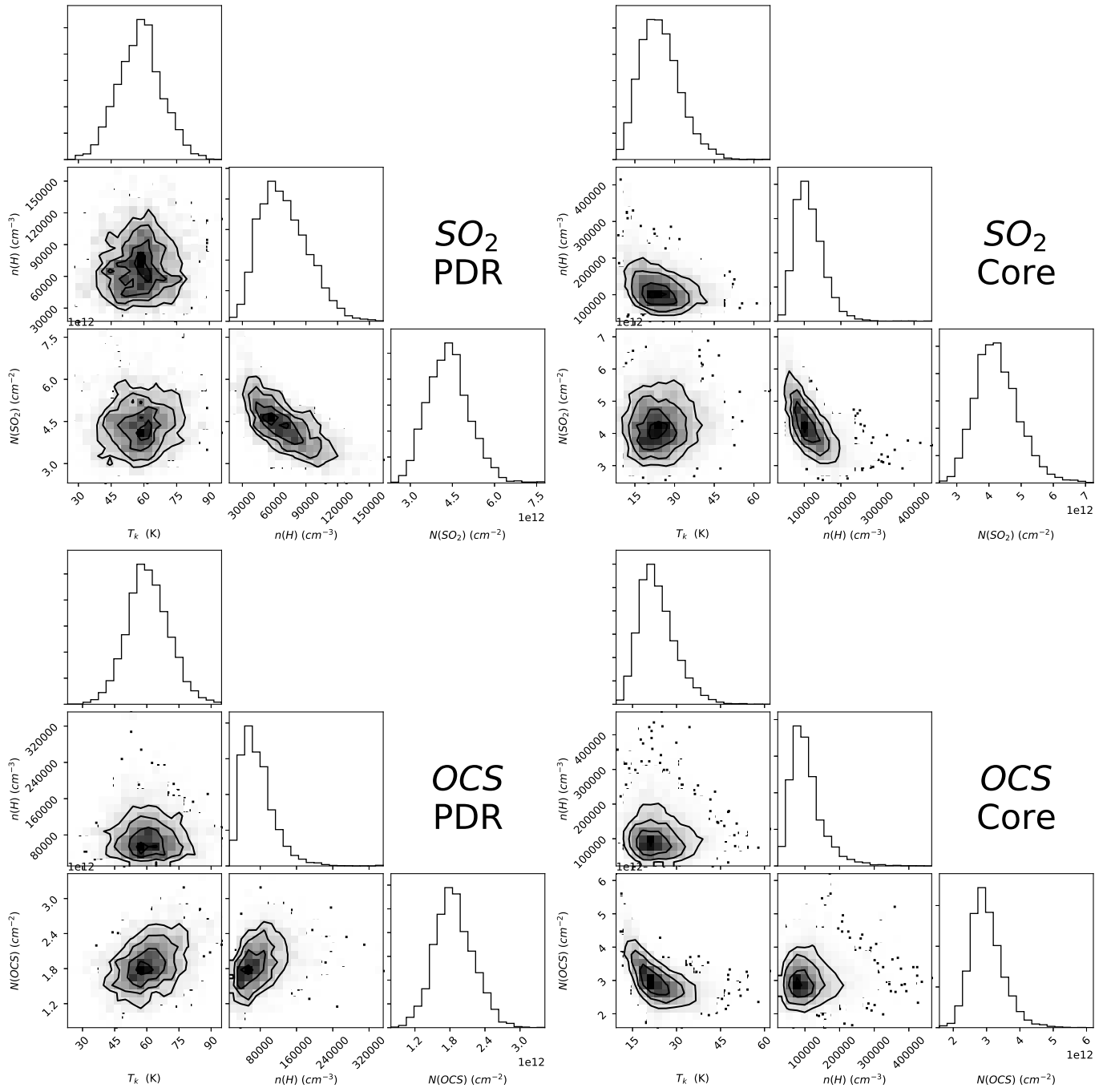


Fig. B.1. Histograms of the MCMC RADEX parameter distribution for the different molecules and regions studied.

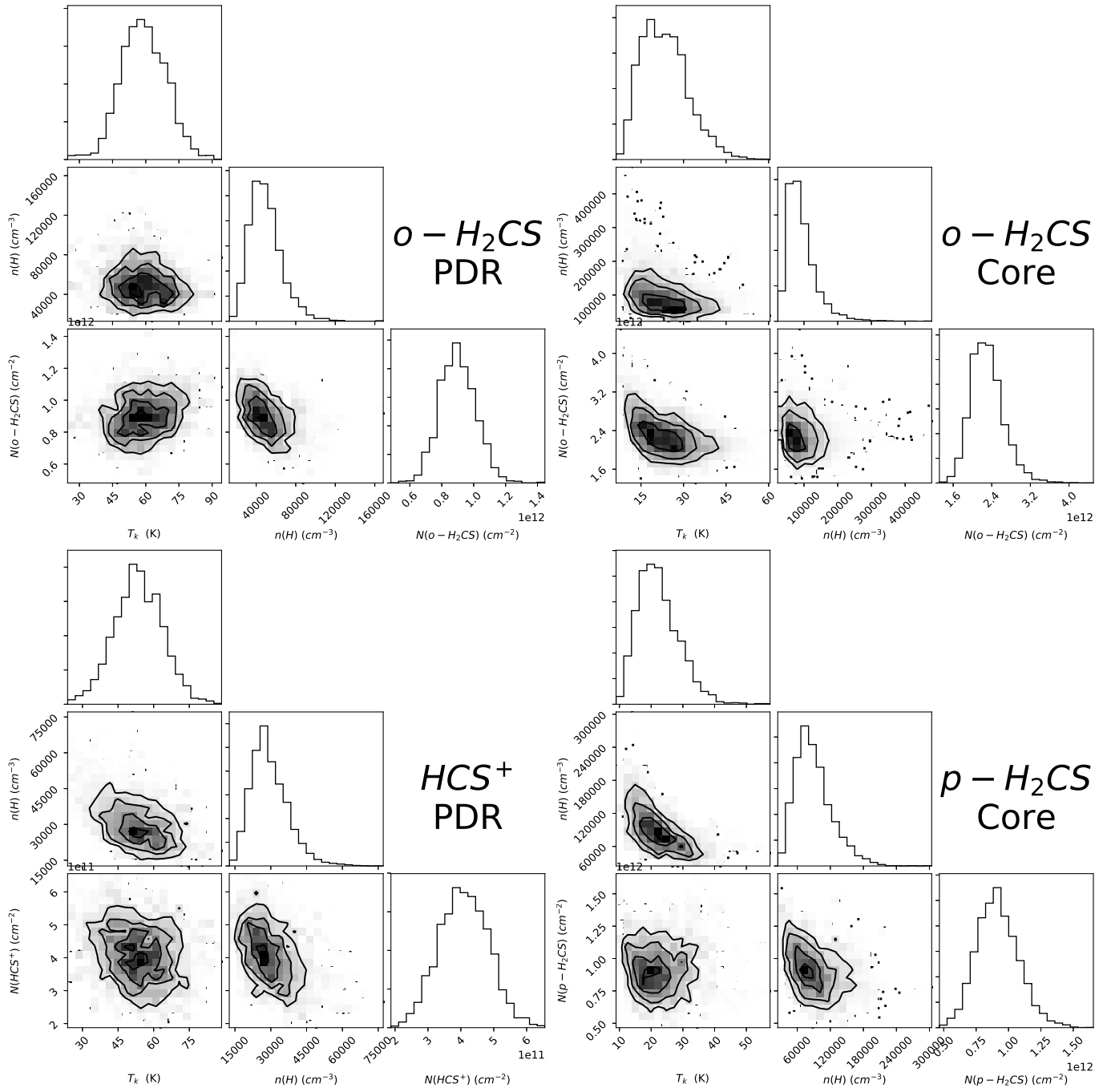


Fig. B.1. Histograms of the MCMC RADEX parameter distribution for the different molecules and regions studied.